Solvent-exchange process in MOF ultrathin films and its effect on CO_2 and methanol adsorption

M. A. Andrés[†#], P. Fontaine[‡], M. Goldmann[‡£], C. Serre[§], O. Roubeau[#], I. Gascón[†#*]

Instituto de Nanociencia y Materiales de Aragón (INMA), CSIC and Universidad de Zaragoza, 50009 Zaragoza, Spain

† Departamento de Química Física, Facultad de Ciencias, Universidad de Zaragoza, 50009 Zaragoza, Spain

‡ Synchrotron SOLEIL, L'Orme des Merisiers, Saint-Aubin, BP 48, 91192, Gif-sur-Yvette, France

£ Institut des NanoSciences de Paris, UMR 7588 CNRS, Sorbonne Université, 4 place Jussieu, 75252 Paris Cedex 05, France

§ Institut des Matériaux Poreux de Paris, FRE 2000 CNRS Ecole Normale Supérieure de Paris, Ecole Supérieure de Physique et de Chimie Industrielles de Paris, PSL Research University, 75005 Paris, France

Corresponding Author

*Ignacio Gascón, E-mail: igascon@unizar.es, Phone number: +34 976761204.

ABSTRACT:

Metal-organic framework (MOF) activation is crucial for the use of MOFs in several applications and solvent-exchange process is a necessary step in many activation methods. In this contribution, we have explored *in situ* MOF monolayer film formation at the air-water interface. Nanoparticles (NPs) of the Al trimesate MIL-96(Al) retain chloroform into their micropores, which considerably diminishes the CO_2 adsorption capacity of MOF films. However, a solvent-exchange process between chloroform and water increases CO_2 film adsorption capacity by a 30%. Total Reflection X-Ray Fluorescence (TRXF) allows studying the kinetics of this process at the air-water interface, that strongly depends on the NP size. The conclusions derived from *in situ* studies allow optimizing the *ex situ* activation procedure of MIL-96(Al) films deposited onto quartz crystal microbalance (QCM) substrates in order to maximize CO_2 and methanol adsorption.

Keywords: metal organic framework (MOF), MIL-96(Al), nanoparticles (NPs), Langmuir and Langmuir-Blodgett (LB) films, quartz crystal microbalance (QCM), adsorption studies, CO_2 adsorption, VOC adsorption, synchrotron characterization.

1.- INTRODUCTION

Metal-organic frameworks (MOFs) are nowadays ubiquitous in scientific research, with even their own subset in the Cambridge Crystallographic Data Centre (CCDC) [1-5]. Undoubtedly, one of the most relevant properties of MOFs is their high porosity, basic for their use in separation processes[6,7], gas storage[8,9], catalysis[10-12], sensing[13,14], drug delivery[15-17] and many others. Usually, as-synthesized MOFs contain guest molecules, such as solvents, unreacted components and other chemicals used in the synthetic procedure, and it is necessary to remove these guest species through an activation process to access the whole MOF porosity[18]. Consequently, different strategies have been developed in order to achieve complete guest removal, preserving the structural integrity of the MOF. Guest exchange using low boiling point and/or low surface tension solvents before thermal treatment under vacuum is currently the most commonly used method in MOF activation[18], although other methods like supercritical CO_2 drying, freeze drying, microwave, chemical or photothermal activation are also used[19,20].

A proper MOF activation is key, but other requirements are also necessary in many MOF applications. In particular, the formation of dense and homogeneous MOF films onto surfaces is required for the development of several MOF-based devices[21]. In previous studies[22-24], some of us have shown the fabrication of compact and dense monolayer films at the air-water interface formed by nanoparticles (NPs) of size ca. 200 nm from the microporous Al trimesate MIL-96(Al) (MIL stands for Materials from Institut Lavoisier). The Langmuir-Blodgett (LB) technique allows the subsequent deposition of these monolayers onto substrates of different nature and shape, such as glass, quartz, mica, QCM disks, solid state interdigitated electrodes and fabrics containing textile electrodes. Moreover, MIL-96(Al) LB films have been used as active layer of methanol and humidity sensors and also to study CO_2 adsorption and desorption processes. An interesting conclusion from these studies[22] was the significant increase (around 30%) of the CO_2 adsorption capacity of LB films deposited onto QCM disks, achieved by disk immersion into water or methanol during 12 h just after film preparation. This suggests that film immersion into these solvents could produce suppression of surface barriers together with the solvent-exchange of retained chloroform molecules within MOF pores.

In order to further investigate water-chloroform solvent-exchange processes on MOF ultrathin films and its effect on film sorption capacity, films formed by MIL-96(Al) NPs of two different sizes (ca. 100 and 200 nm) have been investigated in this contribution. *In situ* synchrotron characterization during film formation at the air-water interface has allowed studying how the K_α chlorine X-ray fluorescence signal from retained chloroform in the film decreases during film formation. Finally, the CO_2 and MeOH adsorption capacity of the films has been evaluated using a QCM-based setup.

2.- MATERIALS AND METHODS

2.1.-MOF synthesis and characterization

Spherical NPs of 100 and 200 nm of MIL-96(Al) were prepared following a procedure previously reported by some of us[22,25]. Nanoparticle size and shape were controlled by the molar ratio of reactants, the solvent mixture composition (H_2O/DMF instead of pure H_2O) and the use of acetic acid as modulator. Briefly, for 100 nm NPs, 2.25 g of aluminum nitrate nonahydrate (Merck, 98.5%) and 1.26 g of trimesic acid (Sigma Aldrich, 95%) were added to 300 mL of an H_2O/DMF (volume:volume = 1/1) mixture. Then, 0.84 mL of acetic acid (Sigma Aldrich, 99.7%) were added. The mixture was continuously stirred and heated under reflux for 16 h. A milky suspension was obtained and MOF powder was centrifuged (14500 rpm, 15 min) and washed first with deionized water, then with a 1:1 H_2O:EtOH mixture, and finally with pure EtOH (30 mL of each). The obtained white powder was finally dried in air at room temperature. NPs of 200 nm were synthesized following the same protocol but with twice the reagent concentrations.

CO_2 adsorption isotherms of the NPs were determined in a Micromeritics ASAP 2020 equipment at 303 K with a water bath as a coolant. N_2 sorption was registered at 77 K using a Quantachrome Autosorb-6 equipment. In both cases, MOF powder was activated at 150 °C for 12 h under vacuum.

H_2O and MeOH vapor sorption analysis were conducted at 298 K using a volumetric Quantachrome VStar4 equipment and $CHCl_3$ sorption was analyzed in a Quantachrome Vstar. MIL-96(Al) NPs were activated *in situ* at 150 °C (H_2O and MeOH) or 100 °C ($CHCl_3$) under vacuum for 16 h.

Powder X-Ray Diffraction (PXRD) was registered with a Bruker D8 diffractometer with a rotating capillary (θ−2θ) using Cu radiation ($\lambda K_{\alpha 1}$ = 1.54059 Å).

Scanning Electron Microscope (SEM) images were registered using a FEI Inspect F50 FE-SEM operated at 10 kV. Before specimen inspection, samples were coated with a conductive layer of platinum (5-10 nm).

2.2.- Langmuir and Langmuir-Blodgett film fabrication and characterization.

A NIMA 702BAM Langmuir trough (720 × 100 mm) with a symmetrical double-barrier configuration was used for film characterization at the air-water interface (π–A isotherms).

Additional film characterization was performed in this device, including surface potential measurements (ΔV) and Brewster Angle Microscopy (BAM).

Langmuir-Blodgett (LB) films were fabricated using a KSV NIMA trough, model 2000-System 3 (775 × 120 mm) also arranged in a symmetrical double-barrier configuration.

Both troughs were placed inside closed cabinets in a dedicated facility to limit the presence of dust and at constant temperature (20 ± 1 °C). Ultra-pure Milli-Q water (ρ = 18.2 MΩ·cm) was used in all the experiments as subphase. Films were compressed in all cases at a constant speed of 6 cm^2/min and surface pressure was continuously monitored by means of a Wilhelmy balance using a filter paper plate.

BAM images were acquired using a KSV NIMA Micro BAM equipped with a red laser (50 mW, 659 nm) as light source. The incidence angle was fixed at 53.1° and a black quartz plate was placed inside the trough as a light trap. The optics of the system provided a spatial resolution of 6 μm per pixel in the water surface plane and a field of view of 3600 x 4000 μm^2. Surface potential-area isotherms (ΔV–A) were registered using a KSV NIMA SPOT surface potential sensor.

MIL-96(Al) NPs suspensions of 0.2 mg/mL were prepared using chloroform (Macron, >99.8%) as solvent and dry MOF powder. Suspensions were sonicated using an ultrasonication probe-type device Hielscher UP400S (Power output 400 W) equipped with an H3 type tip (3 mm diameter). Different sonication times and amplitudes were used: 30 minutes at 50% amplitude for 200 nm NPs and 60 minutes at 70% amplitude for 100 nm NPs. In both cases, the samples were sonicated continuously and prepared suspensions were sonicated for 30 min in an ultrasound bath before the spreading process at the air-water interface.

Dynamic Light Scattering (DLS) experiments were conducted in a Malvern Zetasizer Nano ZS ZEN3600 equipped with a 633 nm laser and configured in a back-scattering arrangement at 173°. These measurements were used to optimize probe sonication parameters for suspension preparation (see **Supplementary Material, Section 2**). Dispersions were analyzed using square optical glass cuvettes (Malvern, model PCS1115) with an optical path of 10 mm and a volume capacity of 3500 μL. Ultrasound bath sonication for 10 min was used before measurement.

LB films were fabricated onto solid substrates (glass, quartz plates and QCM crystals) by vertical dipping at a surface pressure of 25 mN/m (100 nm NPs) or 30 mN/m (200 nm NPs). Transfer was performed in the emersion direction using a vertical speed of 1 mm/min.

SEM images of LB films were acquired using the FEI Inspect F50 FE-SEM described above.

LB films fabricated onto quartz plates (Hellma Analytics, 665.000-QS, 45 mm × 12.5 mm × 1.25 mm) were analyzed using a Varian Cary 50 spectrophotometer and a normal incident angle with respect to the film plane. UV-Vis spectra were registered in the 200-900 nm range. Quartz cuvettes of 350 µL with 1 mm of light path (Hellma Analytics, 100-QS) were used to characterize the UV-Vis spectra of suspensions.

Grazing Incidence X-ray diffraction (GIXD) analysis was performed on LB and drop-cast films deposited onto Si(100) substrates. A high-resolution Empyrean diffractometer (PANalytical) operated at 45 kV (generator voltage) and 40 mA (tube current, Cu K_α radiation) was used and scans were collected in the open detector mode using a Pixcell 1D medipix3 detector. Grazing incidence angles between 0.13° and 0.16° were used. The value was optimized before each scan.

2.3.- Synchrotron characterization of Langmuir films

Grazing-Incidence X-Ray Diffraction (GIXD), Grazing-Incidence Small-Angle X-Ray Scattering (GISAXS) and Total Reflection X-ray Fluorescence (TRXF) studies at the air-water interface were performed at SIRIUS Beamline of the SOLEIL Synchrotron (Saint Aubin, France) [26]. The measurements were performed using an incident X-ray beam of 8 keV ($\lambda = 0.155$ nm), a beam size of 0.1 × 0.5 mm^2 (V × H), and an incidence angle of 2.0 mrad with the water surface below the total external reflection critical angle value of the air-water interface (2.7 mrad at 8 keV). GISAXS measurements were done using a 2D PILATUS3 1M (Dectris, Switzerland) detector located at 4.5 m from the sample. A vertical tungsten rod is used as a beam-stop for the direct and reflected beams. A flight path tube flushed with helium gas is located between the sample and the detector in order to reduce absorption and scattering by air.

The GIXD setup uses a 2D PILATUS2 (Dectris, Switzerland) detector combined with a Soller collimator of 0.06 degree resolution. This detection setup is continuously scanned over the horizontal 2θ angle in order to record the vertical distribution of intensity that is Q_z-integrated to obtain the diffraction spectra.

Monolayers were prepared in a dedicated Langmuir trough[26] of size 484 × 150 mm. It was enclosed in a gas-tight chamber flushed by Helium gas flow to reduce gas scattering and to avoid the damage of the monolayer by the beam. Temperature was kept constant thanks to a water circulating bath at 20 ± 1 °C.

X-ray fluorescence measurements were done either by a four element silicon drift detector (XFlash QUAD 504, Brüker, Germany) mounted almost horizontally on the side of the liquid

surface (experiments labeled A in Table 1) or a one element silicon drift detector (XFlash 430 M, Brüker, Germany) equipped with a collimator and mounted at 30° with respect to the vertical direction towards the X-ray source in order to reduce the elastic peak that would otherwise saturate the detector (experiments labeled B in Table 1). Data were normalized by the initial intensity in each experiment and the mass density of the MOF at the air-water interface at each time.

Normalized fluorescence evolution was adjusted using two exponential models:

$$\underline{\text{Single stretched exponential model:}}\ I = I_\infty + A_1 e^{-(t/\tau_1)^\beta}$$

$$\underline{\text{Biexponential model:}}\ I = I_\infty + A_1 e^{-t/\tau_1} + A_2 e^{-t/\tau_2}$$

where I corresponds to the normalized relative fluorescence intensity at each t time, A_1 and A_2 are pre-exponential factors, β is the stretching factor, I_∞ is the asymptotic fluorescence value at long times (close to infinite), and τ_1 and τ_2 correspond to the characteristic times of the processes under modeling.

2.4.- QCM-based setup for gas/vapor adsorption studies

Gas adsorption measurements were performed using a homemade QCM-based experimental setup previously described in the literature by some of us[22,27]. Briefly, it consists of a stainless steel cell (ca. 200 mL volume capacity) which contains two chlorinated polyvinyl chloride CHC-15 crystal holders from Inficon (**Figure S16b**). Each of these holders is connected through a 2´ SMB-SMB plug to a Phase Lock Oscillator (5.1-10 MHz range). Both phase lock oscillators were placed inside an Inficon RQCM system. AT-cut QCM disks of 9 MHz and 1 inch in diameter were purchased from Inficon (ref. 149272-1) and QuartzPro (ref. QCM9254CrA128-064-M) and one disk was coated with the thin film and the other used as a reference to correct fluctuations from temperature, pressure or gas flow changes. The measurement chamber is also equipped with two electric resistors and two thermocouples to control temperature during the experiment. The pressure was also monitored using a pressure sensor.

Gas adsorption experiments were performed using two separately controlled MC-100SCCM-D/5M Alicat Scientific mass-flow controllers (MFCs), each one either for the diluting gas (Helium, Air Liquide Alphagaz 1, ≥ 99.999% in volume) or the adsorbate (CO_2, Air Liquide N48, ≥ 99.998% in volume). A total gas flow of 50 mL (STP)/min was used in these experiments. Gas adsorption experiments were conducted at constant temperature (303 K) and a total pressure of

100 kPa using five different CO_2 partial pressures in the gas mixture corresponding to 20%, 40%, 60%, 80% and 100% in volume.

The QCM-based setup was modified in order to perform vapor sorption experiments at constant temperature (298 K). A detailed description including the verification of the system using a reference material is included in the **Supplementary Material, Section 5 (Figures S14 to S16)**. Briefly, two independent Alicat Scientific MFCs (MC-100SCCM-D/5M) were used in these studies, one of them for the dilution stream (pure Helium) and the other to generate saturated vapors (see Scheme in **Figure S16a**). For that purpose, Helium was bubbled through a perfluoroalkoxy polymer (PFA) bubbler (Bola Gaswasch-Flaschen A118-01) with a total capacity of 250 mL containing methanol to generate a saturated vapor stream. This bubbler was immersed into a glass cooling vessel of 500 mL with a water jacket (Vidrafoc 505/5) connected to a Huber Minichiller thermostatic circulator set at 281 K. Vapor was considered to be saturated at the chiller temperature. The saturated current was further equilibrated at the chiller temperature and then mixed with the diluting current before entering the measurement chamber. A total gas flow of 100 mL (STP)/min was used in these experiments. To minimize vapor condensation in the pipes, the saturated current was always kept below 60 mL/min.

Vapor concentration in the cell was calculated as relative pressure ($p/p°$) using the following formula and considering that the vapor stream was saturated at the chiller bath temperature:

$$\frac{p}{p^\circ} = \frac{p_{i,T}\dfrac{F_{carrier}}{F_{total}}}{p^\circ}$$

where $F_{carrier}$ is the amount of He flown to the bubbler, F_{total} is the total flow entering the measurement cell, $p_{i,T}$ is the solvent vapor pressure at chiller bath temperature, p is the partial pressure of the vapor inside the cell, and $p°$ is the vapor pressure of the solvent at the measurement temperature. F_{total} can be calculated as:

$$F_{total} = F_{sat.,bubbler} + F_{dilution}$$

where $F_{sat.,bubbler}$ is the flow exiting the bubbler (wet current) and $F_{dilution}$ is the amount of He (dry current) used as dilution before entering the cell. $F_{sat.,bubbler}$ may be calculated as:

$$F_{sat.,bubbler} = F_{carrier} + F_{vapor} = F_{carrier} + \frac{p_{i,T}}{p_{working}} F_{carrier} = \left(1+\alpha\right) F_{carrier}$$

where F_{vapor} is the flow of saturated vapor generated, $p_{working}$ is the working pressure (ambient pressure in this case) and α may resemble a vaporization efficiency.

Before starting each adsorption experiment (CO_2 or MeOH adsorption), the samples were outgassed at 353 K during 2 h under a constant flow of He (50 mL (STP)/min for CO_2 and 100 mL (STP)/min for MeOH) and then cooled to the measurement temperature (303 K for CO_2 and 298 K for MeOH) maintaining the same He flow until a stable frequency was obtained.

Sauerbrey equation [28] was used to determine the mass of the MOF film deposited onto QCM disks prior to gas/vapor adsorption and also to obtain the amount of analyte adsorbed at each adsorbate concentration in the cell during adsorption experiments. This equation relates the change in the frequency of the quartz crystal resonators with mass variation, $\Delta f = -C_f \Delta m$, where Δf is the frequency change in Hz, C_f is the sensitivity factor of the QCM crystal (0.1834 Hz·ng^{-1}·cm^2 for the 9 MHz disks used) and Δm is the change in mass per unit area. MOF mass was calculated from the frequency difference after film deposition. To derive the adsorbed analyte values the frequency differences between the disk before adsorption and after stabilization at each step in the isotherm were evaluated (see **Section 6**, **Figure S17** and **Figure S18** in Supplementary Material). Mass differences were converted into moles of analyte using the molecular weight of either CO_2 or MeOH. At least two different samples were analyzed and average values together with error bars were plotted. Error bars in some points are almost not visible because of the size of the symbols. Finally, at the end of each experiment, pure He was flown to sweep adsorbates from the films and frequency changes were monitored during this procedure in order to confirm sample recovery. A recovery of 95–100% was obtained from the frequency changes in all the experiments.

3.- RESULTS AND DISCUSSION

3.1.- Langmuir and Langmuir-Blodgett films

Spherical MOF NPs of 191 ± 18 and 109 ± 8 nm (**Supplementary Material, Figures S1a,b**) were prepared according to the procedure described in the Materials and Methods section. FTIR-ATR spectra confirmed the absence of unreacted trimesic or acetic acid and the hydrated character of the MOF (**Supplementary Material, Figure S1c**). PXRD patterns were in accordance with the simulated diffractogram[25] and proved the synthesis of crystalline NPs (**Supplementary Material, Figure S1d**). BET area for the smaller NPs was ca. 665 m^2/g (**Supplementary Material, Figure S2a**), close to the value determined for 200 nm NPs (680 m^2/g), reflecting that the porosity of the material does not significantly change with the size decrease.

Initial experiments used diluted suspensions of 100 nm NPs in chloroform (0.2 mg/mL and 0.5 mg/mL) prepared using an ultrasonic processor. Under probe sonication, the effective ultrasonication intensity can be up to 100 times greater than those using conventional ultrasound

baths[29,30]. Similar conditions to those described for 200 nm NPs were used (30 min of continuous sonication at 50% amplitude) [22] but π-*A* isotherms with a remarkable lack of reproducibility and low areas per MOF mass were obtained (**Figure S4**). Hence, sonication process needed to be optimized to improve suspension stability and reduce particle agglomeration. A complete detail of this optimization process is included in **Supplementary Material, Section 2, Figures S4 to S7**.

Under optimal sonication conditions (60 min of continuous sonication at 70% amplitude), reproducible π-*A* isotherms were obtained (**Figure 1a**). Moreover, these isotherms showed similar areas per MOF mass and steep slopes, as for the 200 nm NPs Langmuir films. BAM images obtained during film formation confirmed the formation of dense and compact films (**Figure 2**). Small domains could be observed at areas from 200 cm^2/mg and started to coalesce at a surface pressure of ca. 0.2 mN/m (118 cm^2/mg). Almost full coverage of the water surface was seen around 0.5 mN/m (105 cm^2/mg). Similar images were obtained between 5 and 30 mN/m indicating only small changes in film packing. Finally, the collapse was observed around 35 mN/m. ΔV-*A* isotherms were also in accordance with the formation of a tightly packed NPs film (**Figure 1b**). A decrease in the slope could be observed around 0.5 mN/m in good accordance with almost full coverage of the film. A new slope change leading to an asymptotical value was observed around 37.5 mN/m reflecting film collapse and the formation of 3D aggregates as suggested by BAM images.

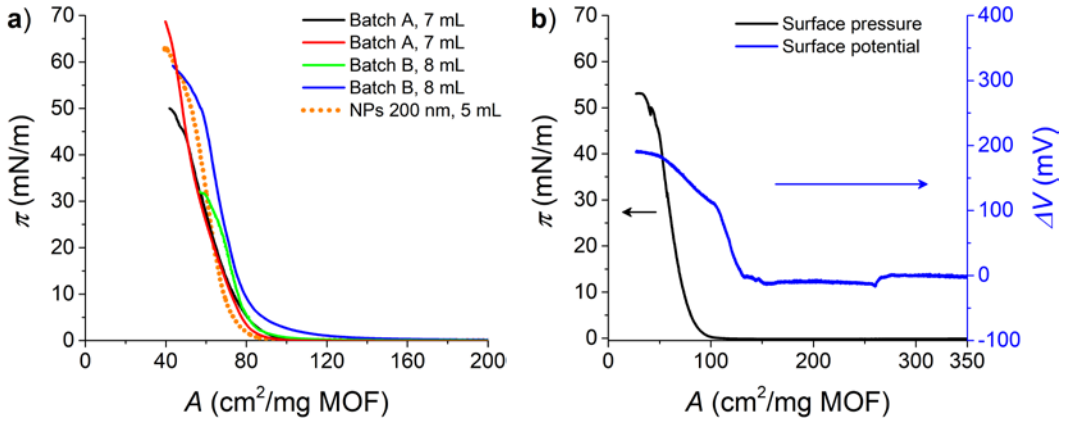

Figure 1. a) Surface pressure-area (π-*A*) isotherms obtained using probe-sonicated suspensions of MIL-96(Al) NPs of 100 nm in chloroform. For comparison purposes, a π-*A* isotherm obtained in optimal conditions for the 200 nm NPs is included (orange dotted line). b) ΔV-*A* isotherm for a 0.2 mg/mL ultrasonicated dispersion of 100 nm MIL-96(Al) NPs (blue line). The corresponding π-*A* isotherm is also shown for clarity purposes (black line). In all cases, samples of 100 nm NPs were sonicated continuously for 60 min at 70% amplitude.

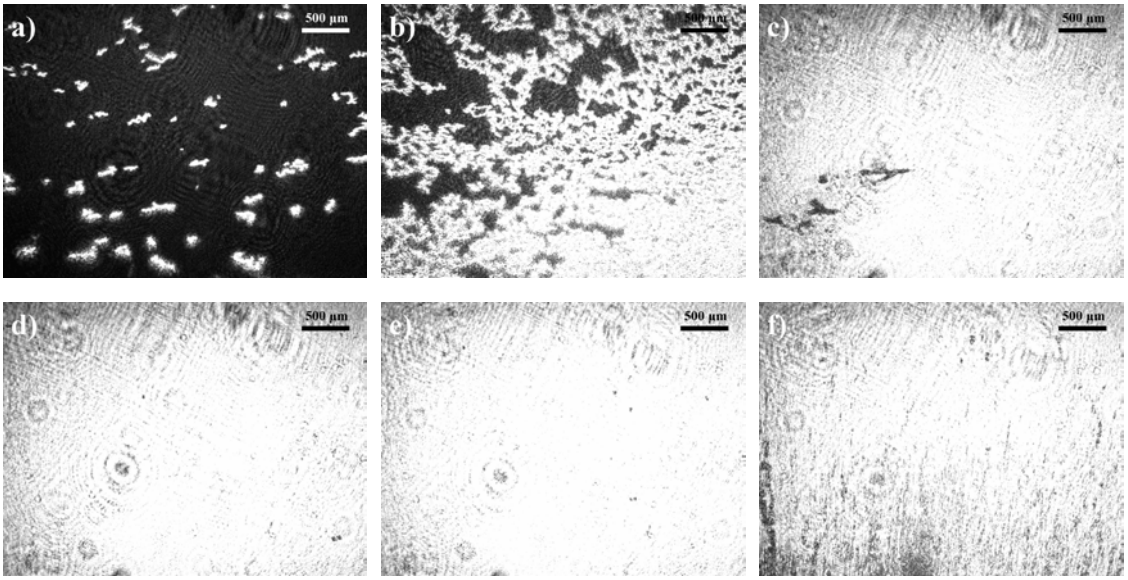

Figure 2. BAM images obtained at the air-water interface at different areas per MOF mass using diluted suspensions (0.2 mg/mL) of 100 nm NPs prepared by continuous probe sonication (60 min, 70% amplitude): (a) 0.0 mN/m (198 cm^2/g), (b) 0.2 mN/m (118 cm^2/mg), (c) 0.5 mN/m (105 cm^2/mg), (d) 5.0 mN/m (81 cm^2/mg), (e) 22.0 mN/m (69 cm^2/mg), (f) 35 mN/m (56 cm^2/mg).

To determine the optimal transfer pressure, LB films of 100 nm NPs were transferred onto glass substrates at different surface pressures in the range between 5 and 30 mN/m, according to the results obtained from BAM images. SEM characterization of these samples (**Figure 3**) showed an increasing surface coverage from 5 to 25 mN/m, with those prepared at 25 mN/m presenting the optimal coating. A further increase to 30 mN/m produced considerable agglomeration, probably formed during LB transfer due to film stiffness. The optimal transfer pressure was lower in comparison to 200 nm NPs (30 mN/m in that case). However, almost defect-free LB films could be also obtained with 100 nm NPs without the need of any additional species (e.g. surfactants[27,31]), showing that MOF particle size may be decreased without impacting LB film quality.

Films were also prepared onto quartz plates in the same conditions to characterize their UV-Vis absorption properties (**Supplementary Material, Figure S8a**). UV-Vis spectra showed a peak (221 nm) and a shoulder (240 nm) from the overlapping of two peaks due to band broadening, probably induced by scattering from the particles. Those peaks can be assigned to π–π^* transitions of the benzene-1,3,5-tricarboxylate rings[32,33]. In addition, they are blue-shifted with respect to the suspension by ca. 5 nm, probably by the polarity change induced by the solvent. Moreover, a displacement to shorter wavelengths is also observed in comparison to 200 nm NPs due to particle size decrease. Intensities were also ca. 2 times lower for 100 nm LB films (**Supplementary Material, Figure S8b**).

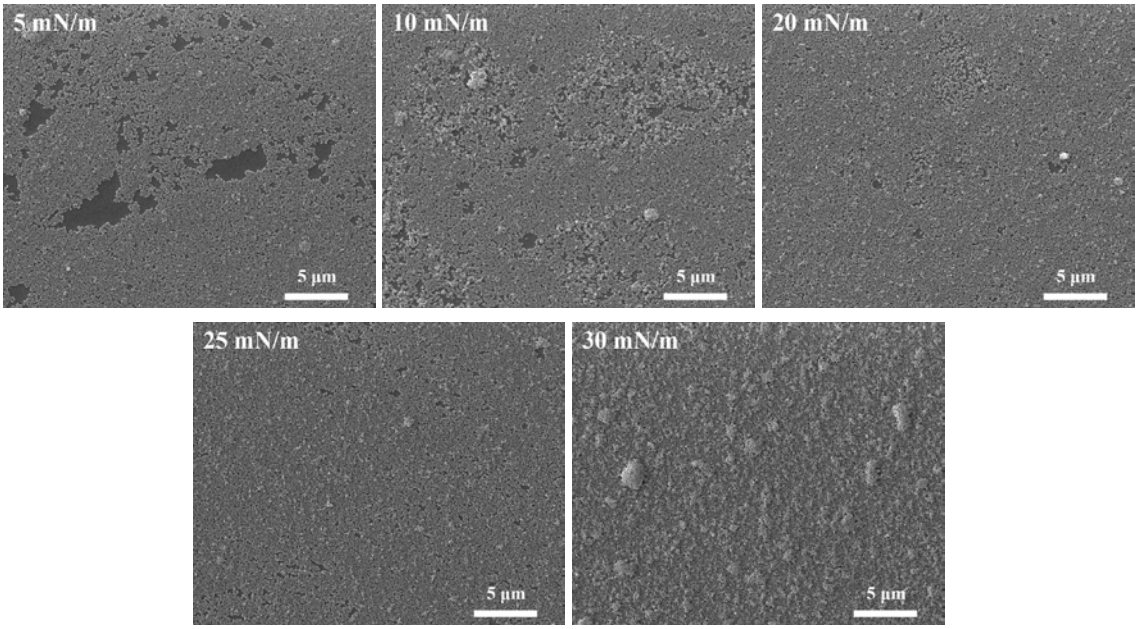

Figure 3. Representative SEM images of LB films of 100 nm NPs transferred onto glass substrates at different surface pressures: 5, 10, 20, 25 and 30 mN/m. Spreading suspensions were prepared in optimal conditions using ultrasonic probe.

3.2.- *In situ* synchrotron studies

In situ GIXD was monitored during film compression for both the 100 and 200 nm MIL-96(Al) NPs (**Figure 4a** and **Figure S9**). Already at low pressure, the characteristic pattern of the bulk material can be observed, in agreement with the NPs maintaining their crystallinity throughout the process of dispersion and LB film formation. Intensities of the peaks increase with increasing pressure, in agreement with the increased density of NPs in the volume sensed by the X-ray beam upon compression. No significant modifications of the GIXD patterns with respect to the bulk solid are observed that could point to a preferential specific orientation of the particles at the gas-water interface. Both 100 and 200 nm NPs are therefore randomly oriented in the Langmuir film, which is reasonable considering their relatively spherical nature. *In situ* Grazing-Incidence Small-Angle X-ray Scattering (GISAXS) patterns were also acquired for both NP sizes to ascertain the potential building of a specific in-plane NP structural organization in the Langmuir film. In both cases, two symmetric maxima arise upon compression, that can be ascribed to the Bragg rods corresponding to the NPs layer (**Figure S10** and **Figure 4b**). The integrated q_z vs. q_{xy} data at 10 mN/m can be reproduced satisfactorily considering a gaussian peak on top of a power-law background (**Figure 4b**), yielding peak maxima of q_{xy} = 0.0674(2) and 0.0375(2) nm^{-1} respectively for the 100 and 200 nm NPs. Assuming an almost hexagonal packing of the NPs, one obtains inter-particle center-to-center distances $D = 4\pi/q_{xy}\sqrt{3}$ of respectively 129 and 232 nm, only slightly larger than the NP size. It indicates that the Langmuir film is already dense and

homogeneous, in agreement with BAM and SEM observations. The absence of modulation of the signal along q_z and of diffraction spots at $q_z > 0$ (see inset in **Figure S10**), that would arise in the presence of multilayer(s), in addition, supports the formation of a purely 2D monolayer organization of the NPs. In the case of the 200 nm NPs, a second weaker peak can be detected at *ca.* 0.067 nm^{-1}, likely corresponding to the 11 peak of the hexagonal packing, expected at $\sqrt{3}$ of the first peak *i.e.* 0.065 nm^{-1}, and thus pointing at a structured layer (**Figure S10c**). The correlation length is however only *ca.* 500 nm, as derived from the Gaussian peak width and Scherrer law. The order is therefore only local, over merely 2-3 NPs lattices, with no long-range order. This together with the weaker scattering intensity of the 100 nm NPs may explain why the second peak is not detected in the case of the smaller NPs. Again, these observations can be reasonably explained by the characteristics of the NPs, with an imperfect spherical shape and a modest but clear size polydispersity, while they are in agreement with the SEM images of transferred layers (**Figure 3**).

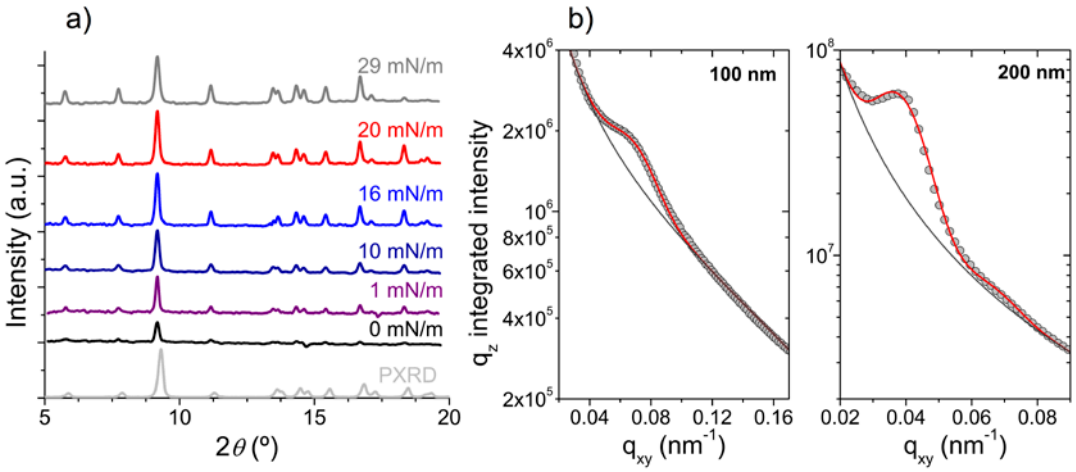

Figure 4. a) *In situ* GIXD patterns for 200 nm MIL-96(Al) NPs at the gas-water interface at increasing pressure, as indicated, compared with the powder patterns of the bulk solid. b) *In situ* GISAXS data for MIL-96(Al) NPs at the gas-water interface at 10 mN/m. The red line is the best-fit of the data to a power-law background ($\sim q^{-2.18}$, as grey dash line) and either one (100 nm NPs) or two (200 nm NPs) Gaussian peak(s) with maxima at q_{xy} = 0.0674(2) and 0.0375(2)/0.067(1) nm^{-1} and width of 0.0191(4) and 0.0096(3) nm^{-1}, respectively.

Total Reflection X-Ray Fluorescence (TXRF) was registered simultaneously to GIXD and GISAXS to analyze film composition during compression. In order to check the hypothesized chloroform exchange at the air-water interface, Cl K_α emission (2.622 keV) was monitored. Considering that no Cl source was used during NPs synthesis and that a purging step with He (ca. 30 min) was performed to ensure chloroform and oxygen evacuation, before starting film compression and data acquisition, the observed Cl K_α contribution should come from $CHCl_3$

retained within the particles. In addition, the fluorescence data have been normalized by the initial intensity in each experiment and the mass density of the MOF at the air-water interface, so that any variation of the Cl K_α signal should be associated with changes affecting the $CHCl_3$ retained in the film. Interestingly, a marked decrease of the Cl fluorescence signal was systematically observed during film compression, in all steps for both 100 and 200 nm NPs (**Figure 5**).

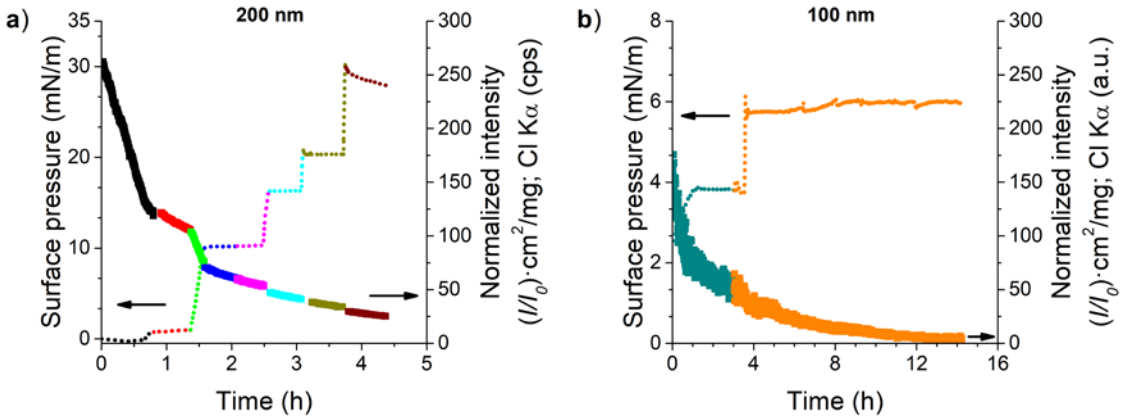

Figure 5. Normalized fluorescence intensity (solid lines) vs. time at the gas-water interface for Cl K_α line for MIL-96(Al) NPs of 200 nm (a) and 100 nm (b). Surface pressure evolution is plotted as dotted lines with the same color coding than fluorescence for each stage. Note that the higher noise observed for the 100 nm NPs experiments arises from the use of a different fluorescence detector than the one employed to characterize the bigger NPs.

MOF NPs presented an adsorption capacity of ca. 6.5 mmol of $CHCl_3$ per MOF gram at 298 K and $p/p° \approx 0.9$. However, the shape of both sorption and desorption branches (**Supplementary Material, Figure S3a**) suggests that the kinetic diameter of the molecules (5.4 Å)[34] hinders the entrance and removal of $CHCl_3$ into and from the pores. Indeed, the desorption branch remained almost flat until enough vacuum was achieved (ca. $p/p° \approx 0.04$) reflecting some kind of confinement effect. Taking into account the high water affinity of the MOF (water adsorption capacity around 13.0 mmol/g at 25 °C and $p/p° \approx 0.2$, see **Supplementary Material, Figure S3c**) and that chloroform solubility in water is significant at this scale (ca. 8 g/L at 25 °C)[35], this suggests a solvent-exchange process with the participation of water. Water is preferentially adsorbed in the accessible free pore volume, dissolving trapped $CHCl_3$ molecules which will diffuse by the gradient difference into the subphase. This phenomenon is typically used during particle post-synthetic activation to remove trapped species and exchange solvent molecules with some others easier to be evacuated afterward[18].

The observed intensity decay was initially faster for 100 nm NPs, in agreement with the higher surface/volume ratio where a higher portion of the particle surface is in contact with the water surface for the solvent-exchange process. To further corroborate our hypothesis, a blank

experiment where only $CHCl_3$ was spread at the air-water interface was conducted and fluorescence was registered after He purging. The obtained results showed an almost constant signal (**Supplementary Material, Figure S11**), and the observed variations were within the noise range, hence proving that the variation of the fluorescence intensity originates from a variation of the adsorbed chloroform into the particles . Moreover, such a phenomenon was also observed for another MOF, MIL-101(Cr)[27,36] (**Supplementary Material, Figure S12**). In this case, the process was faster probably due to the combination of both smaller particle size and much larger pore size (mesoporous MOF) effects.

In order to characterize the kinetics of the proposed $CHCl_3$-H_2O solvent-exchange process, fluorescence data were first fitted to a single stretched exponential model (see **Section 2.3** for details on the used equation). However, this model did not describe accurately the evolution at longer times for the smaller particles or at the beginning of the experiment for the bigger NPs (**Supplementary Material, Figure S13**). Moreover, the obtained values for the stretching parameter β suggested the presence of processes with significantly different characteristic times, τ. In a first approach, at least two processes may coexist. Therefore, a simple biexponential model was explored (see **Section 2.3** for details on the equation). Using this model, a satisfactory simulation was obtained, for both particle sizes (**Figure 6**). The best-fit parameters obtained with both models for all the experiments are summarized in **Table 1**.

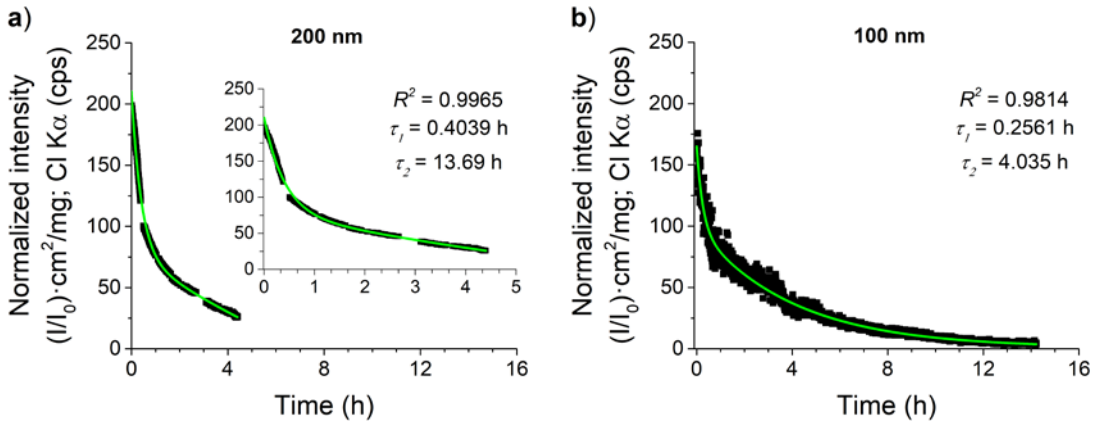

Figure 6. Normalized fluorescence intensity vs. time at the gas-water interface for Cl K_α line for MIL-96(Al) 200 (a) and 100 (b) nm NPs. Inset in a) shows a detail at shorter time scales for clarity purposes. Green lines represent the best-fit of the experimental data to a biexponential model. Fit parameters (R^2, τ_1 and τ_2) are shown in each graph.

Using the biexponential model, a short τ_1 and significantly longer τ_2 were obtained for both NP sizes. Moreover, τ_1 times were shorter for the small particles in all cases (1.8 times on average). Our proposed mechanism considers that τ_1 represents the solvent-exchange process of weakly bound $CHCl_3$ molecules which are either contained near the surface or in more accessible

pores. This suggests that this process would be highly dependent on the surface/volume ratio. Shorter times are obtained for higher surface/volume ratios (e.g. smaller spherical particles) because this process occurs simultaneously on a higher extent of the porous system. On the other hand, τ_2 would mainly represent the removal of strongly bound $CHCl_3$ molecules confined into inner pores in the structure of the MOF NPs. In addition to this effect, τ_2 could also, possibly, include a small contribution from instrumental drift from the detector.

Table 1. Fitting parameters for all the Langmuir film formation experiments of 100 and 200 nm MIL-96(Al) NPs performed in Soleil synchrotron, using either a single stretched exponential or a biexponential model. Experiments were conducted using either a 4 element fluorescence detector (A) or a one element fluorescence detector (B).

		Single stretched exponential model			**Biexponential model**		
	Fluo detector	R^2	β	τ_1 **(h)**	R^2	τ_1 **(h)**	τ_2 **(h)**
200 nm (1)	A	0.9960	0.8520	0.9308	0.9978	0.6742	$2.117 \cdot 10^{5}$ *
200 nm (2)	A	0.9883	0.6793	0.6847	0.9965	0.4039	13.69
200 nm (3)	B	0.8987	1	0.5011	0.9073	0.4661	0.4661[1]
100 nm (1)	B	0.9768	0.4712	2.371	0.9814	0.2561	4.035
100 nm (2)	B	0.9294	0.4723	1.356	0.9384	0.3575	6.283
100 nm (3)	B	0.9598	0.4772	0.259	0.9884	0.2455	4.037

3.3.- Effect of solvent-exchange process on film adsorption capacity

In order to analyze the effect of the solvent-exchange process on film adsorption capacity, LB films of MIL-96(Al) 100 nm NPs were transferred onto QCM substrates at 25 mN/m and CO_2 adsorption was studied and compared with that of the LB films fabricated with 200 nm NPs. Drop-cast samples were also prepared and analyzed to compare adsorption values with those of ordered LB samples (**Supplementary Material, Figure S19**).

Previous FTIR experiments have proved a strong adsorption of CO_2 at the Lewis acid Al^{3+} sites and –OH groups of the structure of MIL-96(Al)[25]. This is reflected on the adsorption

*,1 Fitting to long times was not satisfactory in those cases because measurements were not long enough due to beamline problems. In the first case an abnormally high τ_2 value is obtained, whereas in the second case fitting corresponds to a simple single exponential model $\tau_1 = \tau_2$.

values of CO_2 obtained for the activated bulk material at 30 ºC (ca. 3.2 mmol/g at 1 bar and 6.3 mmol/g at 10 bar) that are among the best performances for small pore MOFs previously reported for CO_2 separation. Moreover, MIL-96(Al) also shows a significant CO_2 adsorption capacity at moderate relative humidity (up to 10%) contrarily to other MOFs. This behavior has been explained by the preferential adsorption of H_2O at low relative pressures on the cavities containing the more hydrophilic groups, which allows CO_2 adsorption on the other cavities containing μ_2-OH groups[37]. The great affinity of MIL-96(Al) for water and methanol at 25 ºC (ca. 5.7 mmol/g for water at $p/p^o \approx 0.03$ and 5.0 mmol/g for methanol at $p/p^o \approx 0.03$) has also been shown in previous studies[22-24,37]. Preferential location of the H_2O and MeOH molecules at low relative pressures is mainly driven by the hydrogen bonding interactions with –OH terminal groups while the differences observed between both compounds at higher relative pressures can be explained by the differences in the kinetic diameters (3.6 Å for methanol and 2.6 Å for water).

CO_2 adsorption for both particle sizes was similar in the bulk form (**Supplementary Material, Figure S2b**). Therefore, under similar activation conditions, the adsorption capacity for LB films was expected to be the same. Interestingly, LB films of both particle sizes showed almost the same adsorption capacity whereas drop-cast samples of the smaller particles presented lower adsorption values (ca. half the value of the bigger particles), with the isotherm presenting a pseudo-linear shape. These results for drop-cast deposits of 100 nm NPs could be reasoned in terms of a worse activation of smaller particles in our experimental setup. Probably the disordered packing of these small particles blocks to a greater extent the surface of the particles, hindering chloroform removal from inside the pores. However, ordered dense and compact packing in LB films leads to the same activation degree for both particle sizes.

Inspired by the results from *in situ* measurements using synchrotron radiation, which proved that the solvent-exchange process could be also performed in Langmuir films, we decided to analyze CO_2 sorption simulating those experiments. For that purpose, firstly films of 200 nm NPs were left at the transfer surface pressure (30 mN/m) at the air-water interface for two different times: 6 or 12 h. After that time, LB films were transferred onto QCM disks and their CO_2 adsorption was determined (**Figure 7a**). Moreover, those results were compared to the measurements previously reported by some of us where films were immersed after transfer either in MeOH or H_2O for 12 h[22] (**Figure 7b**).

The obtained results prove our hypothesis for the solvent-exchange mechanism and show that similar activation degrees were obtained either *in situ* in the Langmuir film or *ex situ* in the immersed LB films. Moreover, 6 h at the air-water interface were also not enough to attain the same degree of activation, like in the immersed film.

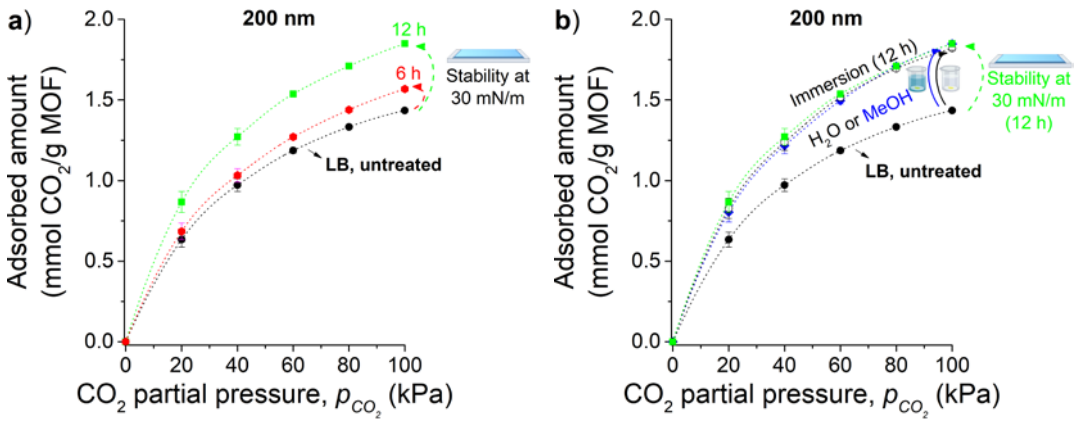

Figure 7. a) CO_2 adsorption isotherms determined at 303 K for 200 nm MIL-96(Al) NPs LB films transferred after 6 h (red ⬢) and 12 h (green ■) in stability at the water surface at 30 mN/m. b) Comparison of CO_2 uptakes on pristine films immersed during 12 h in H_2O (black ○) or MeOH (blue ◆) prior to measurement with the values determined for films after stability for 12 h at the air-water interface (green ■). In both graphs, a plot for pristine LB samples (black ●) is included for comparison purposes. Error bars are standard deviations obtained from the analysis of at least two samples.

As shown in the previous section, the solvent-exchange process was faster for smaller particles. In order to check for this effect of particle size, we conducted CO_2 adsorption measurements on LB films of 100 nm NPs transferred after a stability time of 12 h at the air-water interface. Results showed that adsorption was almost identical to untreated samples (**Supplementary Material, Figure S20**). A fast screening performed into immersed drop-cast samples showed that the optimal time was around 3 h (**Supplementary Material, Figure S21**). Those results together with the fact that drop-cast adsorption for the smaller particles was almost 2 times smaller than the bigger ones, suggested that, probably, the $CHCl_3$ content on pristine LB films of smaller particles is lower than in 200 nm NPs, due to the faster H_2O-$CHCl_3$ exchange.

On the other hand, the experimental QCM-based setup was modified to measure the adsorption of organic vapors on the films. MeOH sorption was characterized on drop-cast and LB film samples of 100 and 200 nm NPs. As MeOH and H_2O molecules compete for the same active sites in the MOF pores, each sample was measured for three successive adsorption-desorption cycles to verify the extent of material activation and study the influence of film ordering. Results for LB films showed that adsorption capacities for both NPs sizes were also identical (**Figure 8**), like in the case of CO_2. Moreover, adsorption for the three cycles was similar, with the one for the first cycle being only slightly lower probably due to some retained H_2O that is swept after completing the adsorption/desorption cycle. Adsorption capacities were ca. 3 times lower in comparison to the bulk due to the limited activation conditions in our setup. Despite this, deposits could be completely regenerated without applying vacuum as evidenced by the desorption branches

(**Supplementary Material, Figure S22**). The degree of activation of the material was reproducible as demonstrated by the almost negligible deviations obtained from the measurement of different samples. In addition, the effect of immersion activation on the adsorption capacity was analyzed. In this case, smaller adsorption capacities were obtained for the 1st cycle, whereas similar or higher adsorption values were obtained for the 2nd and 3rd cycle respectively (**Supplementary Material, Figure S23a**). This can be reasoned considering that MeOH and H_2O molecules compete for the same adsorption sites. Therefore, there is a compromise between H_2O pre-adsorption and the solvent-exchange process for $CHCl_3$. Water molecules are progressively removed during successive adsorption cycles, hence the higher adsorption values in comparison to pristine samples after the 1st adsorption cycle.

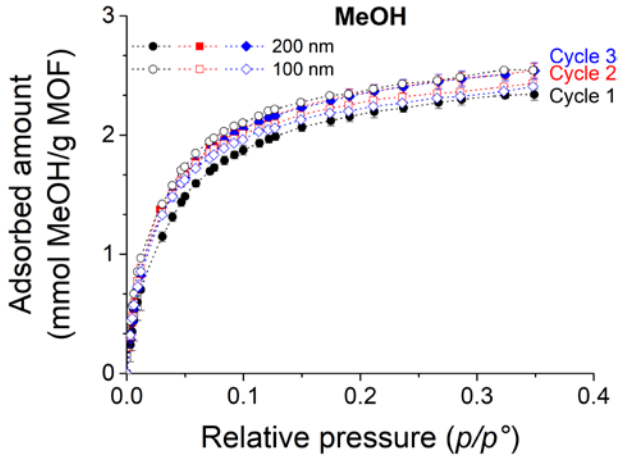

Figure 8. MeOH vapor adsorption isotherms determined at 298 K for LB films of 100 (unfilled symbols) and 200 (filled symbols) nm MIL-96(Al) NPs prepared in optimal conditions. Uptakes were determined for three successive adsorption/desorption cycles: cycle 1 (black ●,○), cycle 2 (red ■,□) and cycle 3 (blue ◆,◇). Saturated MeOH vapors were generated at 281 K. Error bars are standard deviations obtained from the analysis of at least two samples.

Finally, the effect of film ordering on the adsorption of MeOH was also characterized. Lower adsorption capacities and higher variability were obtained with drop-cast samples in all cycles (**Supplementary Material, Figure S23b**) in comparison to LB films. Such variability was not observed in the case of CO_2 adsorption on drop-cast samples. Lower adsorption values may be reasoned by the fact that film disorder creates diffusive barriers that hinder pore evacuation. The same effect was reported previously on CO_2 adsorption experiments, where drop-cast samples also showed lower adsorption capacities in comparison to LB films[22]. On the other hand, the higher variability for all the adsorption cycles may indicate that part of the species not removed due to the poorer activation are swept during the adsorption cycles. These species could present favorable interactions within the pores and cannot be removed with pure He or CO_2 sweeping

during cycling experiments. All these results prove again the importance of film ordering on thin film activation and adsorption properties.

4.- CONCLUSIONS

The fabrication of Langmuir and Langmuir-Blodgett films made of NPs of different size (191 ± 18 and 109 ± 8 nm) of the microporous Al trimesate MIL-96(Al) and their activation through a solvent-exchange process has been studied in this contribution.

We have shown that it is possible to study *in situ* chloroform-water solvent-exchange kinetics at the gas-water interface using synchrotron Total Reflection X-Ray Fluorescence (TRXF). Chloroform retained into MOF pores is released during film formation and Cl K_α signal continuously decreases. This process can be described by a biexponential model, characterized by a short (τ_1) and a significantly longer (τ_2) characteristic times, which are ascribed to, respectively, the solvent-exchange process of weakly bound chloroform molecules and the progressive removal of strongly bound chloroform molecules (probably including a small contribution from instrumental drift from the detector). Moreover, τ_1 times are shorter for the small particles, due to the different surface/volume ratio for both particle sizes.

The activation of the MOF film either *in situ* (films left at the air-water interface at the surface pressure of transference before LB film deposition) or *ex situ* (LB films deposited onto QCM disks and, afterwards, immersed into water) leads to similar CO_2 adsorption values in a QCM-based setup, proving that film activation can be optimized with an adequate study of the solvent-exchange processes. Moreover, methanol adsorption on LB films is larger and shows a better reproducibility than on drop-cast films, revealing that film ordering achieved with the LB method is particularly interesting for the study of gas and VOC adsorption-desorption processes and the development of gas sensors based on MOF films.

Supplementary Material

Figures showing additional details for MOF characterization, MOF NPs suspension optimization, Langmuir and Langmuir-Blodgett film formation and characterization, GIXD/GISAXS/TXRF *in situ* experiments using synchrotron radiation and CO_2 and MeOH adsorption studies using the QCM setup can be found in the online version. A detailed description of MOF NPs suspension optimization protocol and the modification of the QCM gas setup to measure vapors are also included. Supplementary data associated with this article can be found, in the online version, at XXXXXXX.

Acknowledgements

We acknowledge the financial support from the European Union Seventh Framework Programme (FP7/2007-2013) under grant agreement number 608490, project M^4CO_2; and also financial support from Spanish MINECO and FEDER (projects MAT2016-78257-R and MAT2017-86826-R), from the Aragon Government (DGA) and FEDER (research group E31_17R) and from the University of Zaragoza (JIUZ-2015-CIE-02).

M.A. Andrés acknowledges the support of Ministerio de Educación from the Spanish Government under a FPU grant (Formación de Profesorado Universitario, FPU14/05367)

The authors acknowledge the use of the Servicio General de Apoyo a la Investigación-SAI (Universidad de Zaragoza) and the Laboratorio de Microscopías Avanzadas (LMA) at the Instituto de Nanociencia y Materiales de Aragón (INMA, Universidad de Zaragoza and CSIC), for offering access to their instruments and expertise. The authors thank Dr. Guillermo Antorrena for assistance in GIXD experiments. Dr. Inhar Imaz and Dr. Javier Pérez Carvajal are also ackwnoledged for the synthesis of ZIF-8(Zn) NPs and valuable feedback for our experimental QCM-based setup modification.

We thank SOLEIL synchrotron for beamtime provision under the framework of projects 20160935 and 20180164.

REFERENCES

[1] F.-X. Coudert, Responsive metal–organic frameworks and framework materials: under pressure, taking the heat, in the spotlight, with friends, Chem. Mater. 27(6) (2015) 1905-1916.

[2] H. Furukawa, K.E. Cordova, M. O'Keeffe, O.M. Yaghi, The chemistry and applications of metal-organic frameworks, Science 341(6149) (2013) 1230444.

[3] J. Caro, Quo Vadis, MOF?, Chem. Ing. Tech. 90(11) (2018) 1759-1768.

[4] S.L. Griffin, N.R. Champness, A periodic table of metal-organic frameworks, Coord. Chem. Rev. 414 (2020) 213295.

[5] P.Z. Moghadam, A. Li, S.B. Wiggin, A. Tao, A.G.P. Maloney, P.A. Wood, S.C. Ward, D. Fairen-Jimenez, Development of a Cambridge structural database subset: a collection of metal–organic frameworks for past, present, and future, Chem. Mater. 29(7) (2017) 2618-2625.

[6] E. Adatoz, A.K. Avci, S. Keskin, Opportunities and challenges of MOF-based membranes in gas separations, Sep. Purif. Technol. 152 (2015) 207-237.

[7] Q. Qian, P.A. Asinger, M.J. Lee, G. Han, K. Mizrahi Rodriguez, S. Lin, F.M. Benedetti, A.X. Wu, W.S. Chi, Z.P. Smith, MOF-based membranes for gas separations, Chem. Rev. 120(16) (2020) 8161-8266.

[8] Z. Hu, Y. Wang, B.B. Shah, D. Zhao, CO_2 capture in metal–organic framework adsorbents: an engineering perspective, Adv. Sustain. Sys. 3(1) (2019) 1800080.

[9] H. Li, K. Wang, Y. Sun, C.T. Lollar, J. Li, H.-C. Zhou, Recent advances in gas storage and separation using metal–organic frameworks, Mater. Today 21(2) (2018) 108-121.

[10] A. Bavykina, N. Kolobov, I.S. Khan, J.A. Bau, A. Ramirez, J. Gascon, Metal–organic frameworks in heterogeneous catalysis: recent progress, new Trends, and future perspectives, Chem. Rev. 120(16) (2020) 8468-8535.

[11] J. Lee, O.K. Farha, J. Roberts, K.A. Scheidt, S.T. Nguyen, J.T. Hupp, Metal–organic framework materials as catalysts, Chem. Soc. Rev. 38(5) (2009) 1450-1459.

[12] Y.-S. Kang, Y. Lu, K. Chen, Y. Zhao, P. Wang, W.-Y. Sun, Metal–organic frameworks with catalytic centers: From synthesis to catalytic application, Coord. Chem. Rev. 378 (2019) 262-280.

[13] P. Kumar, A. Deep, K.-H. Kim, Metal organic frameworks for sensing applications, TrAC, Trends Anal. Chem. 73 (2015) 39-53.

[14] F.-Y. Yi, D. Chen, M.-K. Wu, L. Han, H.-L. Jiang, Chemical sensors based on metal–organic frameworks, ChemPlusChem 81(8) (2016) 675-690.

[15] L. Gao, Q. Chen, T. Gong, J. Liu, C. Li, Recent advancement of imidazolate framework (ZIF-8) based nanoformulations for synergistic tumor therapy, Nanoscale 11(44) (2019) 21030-21045.

[16] T. Baati, L. Njim, F. Neffati, A. Kerkeni, M. Bouttemi, R. Gref, M.F. Najjar, A. Zakhama, P. Couvreur, C. Serre, P. Horcajada, In depth analysis of the in vivo toxicity of nanoparticles of porous iron(III) metal–organic frameworks, Chem. Sci 4(4) (2013) 1597-1607.

[17] M.-X. Wu, Y.-W. Yang, Metal–organic framework (MOF)-based drug/cargo delivery and cancer therapy, Adv. Mater. 29(23) (2017) 1606134.

[18] J. Ma, A.P. Kalenak, A.G. Wong-Foy, A.J. Matzger, Rapid guest exchange and ultra-low surface tension solvents optimize metal–organic framework activation, Angew. Chem. Int. Ed. 56(46) (2017) 14618-14621.

[19] X. Zhang, Z. Chen, X. Liu, S.L. Hanna, X. Wang, R. Taheri-Ledari, A. Maleki, P. Li, O.K. Farha, A historical overview of the activation and porosity of metal–organic frameworks, Chem. Soc. Rev. 49(20) (2020) 7406-7427.

[20] J. Espín, L. Garzón-Tovar, A. Carné-Sánchez, I. Imaz, D. Maspoch, Photothermal activation of metal–organic frameworks using a UV–Vis light source, ACS Appl. Mater. Interfaces 10(11) (2018) 9555-9562.

[21] V. Stavila, A.A. Talin, M.D. Allendorf, MOF-based electronic and opto-electronic devices, Chem. Soc. Rev. 43(16) (2014) 5994-6010.

[22] M.A. Andrés, M. Benzaqui, C. Serre, N. Steunou, I. Gascón, Fabrication of ultrathin MIL-96(Al) films and study of CO_2 adsorption/desorption processes using quartz crystal microbalance, J. Colloid Interface Sci. 519 (2018) 88-96.

[23] M.A. Andrés, M.T. Vijjapu, S.G. Surya, O. Shekhah, K.N. Salama, C. Serre, M. Eddaoudi, O. Roubeau, I. Gascón, Methanol and humidity capacitive sensors based on thin films of MOF nanoparticles, ACS Appl. Mater. Interfaces 12(3) (2020) 4155-4162.

[24] S. Rauf, M.T. Vijjapu, M.A. Andrés, I. Gascón, O. Roubeau, M. Eddaoudi, K.N. Salama, Highly selective metal–organic framework textile humidity sensor, ACS Appl. Mater. Interfaces 12(26) (2020) 29999-30006.

[25] M. Benzaqui, R.S. Pillai, A. Sabetghadam, V. Benoit, P. Normand, J. Marrot, N. Menguy, D. Montero, W. Shepard, A. Tissot, C. Martineau-Corcos, C. Sicard, M. Mihaylov, F. Carn, I. Beurroies, P.L. Llewellyn, G. De Weireld, K. Hadjiivanov, J. Gascon, F. Kapteijn, G. Maurin, N. Steunou, C. Serre, Revisiting the aluminum trimesate-based MOF (MIL-96): from structure determination to the processing of mixed matrix membranes for CO_2 capture, Chem. Mater. 29(24) (2017) 10326-10338.

[26] G. Ciatto, M.H. Chu, P. Fontaine, N. Aubert, H. Renevier, J.L. Deschanvres, SIRIUS: A new beamline for in situ X-ray diffraction and spectroscopy studies of advanced materials and nanostructures at the SOLEIL Synchrotron, Thin Solid Films 617 (2016) 48-54.

[27] J. Benito, S. Sorribas, I. Lucas, J. Coronas, I. Gascon, Langmuir–Blodgett films of the metal–organic framework MIL-101(Cr): preparation, characterization, and CO_2 adsorption study using a QCM-based setup, ACS Appl. Mater. Interfaces 8(25) (2016) 16486-16492.

[28] G. Sauerbrey, Verwendung von schwingquarzen zur wägung dünner schichten und zur mikrowägung, Z. Phys. 155(2) (1959) 206-222.

[29] J.S. Taurozzi, V.A. Hackley, M.R. Wiesner, Ultrasonic dispersion of nanoparticles for environmental, health and safety assessment – issues and recommendations, Nanotoxicology 5(4) (2011) 711-729.

[30] H.M. Santos, C. Lodeiro, J.-L. Capelo-Martínez, The power of ultrasound. In: Ultrasound in chemistry: analytical applications. 1st ed. Weinheim: Wiley-VCH; 2008, pp. 1-16.

[31] M.A. Andrés, C. Sicard, C. Serre, O. Roubeau, I. Gascón, Ultrathin hydrophobic films based on the metal organic framework UiO-66-COOH(Zr), Beilstein J. Nanotech. 10 (2019) 654-665.

[32] T.-Q. Lu, K.-R. Ma, C. Zhao, Y.-Y. Gu, H.-Q. Su, R.-Q. Li, Solvothermal synthesis, crystal structure and properties of a new bisphosphonic-trimesic acid adduct, J. Iran. Chem. Soc. 12(7) (2015) 1183-1189.

[33] R.K. Vakiti, B.D. Garabato, N.P. Schieber, M.J. Rucks, Y. Cao, C. Webb, J.B. Maddox, A. Celestian, W.-P. Pan, B. Yan, Synthesis and characterization of two- and three-dimensional calcium coordination polymers built with benzene-1,3,5-tricarboxylate and/or pyrazine-2-carboxylate, Cryst. Growth Des. 12(8) (2012) 3937-3943.

[34] J.O. Hirschfelder, C.F. Curtiss, R.B. Bird, The molecular theory of gases and liquids. 1st ed. Hoboken, New Jersey: Wiley; 1954.

[35] D. Mackay, A. Bobra, W.Y. Shiu, S.H. Yalkowsky, Relationships between aqueous solubility and octanol-water partition coefficients, Chemosphere 9(11) (1980) 701-711.

[36] G. Férey, C. Mellot-Draznieks, C. Serre, F. Millange, J. Dutour, S. Surblé, I. Margiolaki, A chromium terephthalate-based solid with unusually large pore volumes and surface area, Science 309(5743) (2005) 2040.

[37] V. Benoit, N. Chanut, R.S. Pillai, M. Benzaqui, I. Beurroies, S. Devautour-Vinot, C. Serre, N. Steunou, G. Maurin, P.L. Llewellyn, A promising metal–organic framework (MOF), MIL-96(Al), for CO_2 separation under humid conditions, J. Mater. Chem. A 6(5) (2018) 2081-2090.